Deployment Dynamics of Thin-Shell Space Structures

Antonio Pedivellano * and Sergio Pellegrino.†
California Institute of Technology, Pasadena, CA, 91125.

This study was motivated by the desire to develop accurate simulation models for the deployment dynamics of future, ultralight deployable structures consisting of multiple thin shells packaged elastically, through a combination of folding and coiling. The specific problem studied is the packaging and unconstrained deployment of a rectangular space frame formed by two thin-shell longerons connected by multiple transverse rods, and called a strip. The study included experiments on high quality test articles, using a suspension system with low inertia and friction. The elastic folds in the strips were tracked with high speed 3D Digital Image Correlation for deployment both in air and near-vacuum. The study also developed a high-fidelity finite element model of the strips that captures the elastic, localized deformation that occurs during the initial folding, the self-contact between different parts of the structure as the folding develops, and the strain energy stored during the folding process. This model accurately captured the deployment dynamics and self-latching of the strips, as well as the effects of air on deployment.

*

Nomenclature

b_1	=	linear bulk viscosity
c_D	=	drag coefficient
c_s	=	stagnation pressure coefficient, kg/m^3
c_V	=	viscous pressure coefficient, $kg/\ s\ m^2$
D	=	aerodynamic drag
$\mathbf{D}$	=	material tangent stiffness matrix, N/mm^2
$\mathbf{D_t}$	=	material tangent stiffness matrix of a taut membrane, N/mm^2
$\mathbf{D_w}$	=	material tangent stiffness matrix of a wrinkled membrane, N/mm^2
$\mathbf{D_s}$	=	material tangent stiffness matrix of a slack membrane, N/mm^2

*Graduate Student, Graduate Aerospace Laboratories, 1200 E. California Blvd, MC 105-50. AIAA Student Member. Currently at: Deployables Cubed GmbH, Burgweg 6, 82110 Germering, Germany. E-mail: apedivel@gmail.com

†Joyce and Kent Kresa Professor of Aerospace and Civil Engineering, Graduate Aerospace Laboratories, 1200 E California Blvd. MC 105-50. AIAA Fellow. E-mail: sergiop@caltech.edu. Corresponding author.

*Presented at Scitech 2021, paper AIAA 2021-0299.

E = Young's modulus, Pa

F_n = normal force on pulley, N

g = gravity acceleration, m/s^2

h = height of counterweight, mm

H_0 = initial height of center of the strip, mm

I_p = moment of inertia of pulley, $kg\ m^2$

L = length of half strip, mm

L_f = distance between pulleys, mm

k = mass scaling factor

M = mass of counterweights, g

m_a = added air mass, g

M_b = bending moment, Nmm

m_k = mass of membrane, g

M_{tot} = $M_1 + M_2$, g

M_1, M_2 = masses at the ends of the cord in the suspension system, g

$\mathbf{n}$ = element normal vector

r = radius of longeron flange, mm

R = radius of pulley, mm

s = curvilinear abscissa along strip, mm

$\mathbf{T}(s)$ = local tangent to longeron

T_f = friction torque in pulley bearing, $N\ mm$

$\mathbf{v}$ = element velocity vector, m/s

V_a = air velocity, m/s

w = web width, mm

W = strip width, mm

z_a = height of air volume, mm

α = angle of longeron flange, $^\circ$

β = rotation of pulley, $^\circ$

ΔM = $M_2 - M_1$, g

$\Delta\Psi$ = nodal material flow of connector element, mm

ϵ_x, ϵ_y = normal strain components in $x - y$ frame

ϵ_1, ϵ_2 = principal in-plane strain components

γ_{xy} = shear strain components in $x - y$ frame

λ_0 = non-dimensional initial half-distance between folds

$\kappa(s)$ = longitudinal curvature of longeron at s,$1/mm$

ν = Poisson ratio

ρ_a = standard air density, kg/m^3

$\theta(s)$ = angle between tangent to a longeron at s and global x-axis, $^\circ$

θ_0 = initial fold angle, $^\circ$

ξ = non-dimensional curvilinear abscissa on the strip

I. Introduction

For many years, deployable space structures forming large planar surfaces have mostly consisted of rigid panels connected by hinges. Packaging of these structures involves folding the panels around the hinges, and deployment is driven either by external mechanisms or by the release of the strain energy stored in the hinges. Two well-known folding schemes are Z-folding, which involves alternating mountain and valley folds in an accordion-like fashion and has been used in many structures, including the initial set of solar arrays of the International Space Station [1], and tri-folding, in which the panels are folded in the same direction; typically, there is a central panel on top of which two side panels are folded, hence the name of this scheme. This folding method has been used in several Cubesats, including MarCO [2] and OMERA [3], and it has also been combined with Z-folding in the Folded Integrated Thin Film Stiffener (FITS) array, demonstrated in the TacSat-2 mission [4].

Alternative approaches for hinge-free deployable structures, with reduced mechanical complexity and potentially lower mass, have clustered around rollable solar arrays and solar sails. These structures consist of a pair of parallel coilable booms supporting a flexible blanket, or four diagonal booms that stretch out a reflective film. The Roll-Out Solar Array (ROSA) flight test [5] demonstrated a flexible blanket containing solar cells and supported by two thin-shell composite slit tubes. This 5.4 m $\times$ 1.7 m array was coiled on a cylindrical mandrel, and self-deployed by the controlled release of elastic strain energy in the deployable booms. The technology demonstration OrigamiSat-1 developed a 1 m $\times$ 1 m membrane deployed by four diagonal open section carbon fiber reinforced plastic (CFRP) thin shell booms [6] which was partially covered with copper indium gallium selenide (CIGS) cells and shape memory alloy antennas.

Recent advances in solar cells, e.g. perovskite cells [7], and flexible electronics [8] have provided the impetus to develop new ultralight structural concepts that can be scaled over a wide range of sizes. The Caltech Space Solar Power Project (SSPP) spacecraft architecture [9] envisages large deployable structures consisting of multiple thin shells that are packaged elastically, through a combination of folding and coiling. The present study was motivated by the desire to develop accurate simulation models for the deployment dynamics of future deployable structures of this kind.

These models have been successfully applied to deployment simulations of small scale prototypes of a complete SSPP spacecraft [10].

Therefore, the specific problem that is studied in this paper is the packaging and unconstrained deployment of a ladder-type, rectangular space frame formed by two thin-shell longerons connected by multiple transverse rods, and called a strip. Figure 1 shows the packaging concept for a strip, which is similar to the previously mentioned tri-fold scheme and involves four symmetrically arranged elastic folds, two in each longeron. An experimental and computational study of the deployment dynamics of strips folded in this way is presented in this paper.

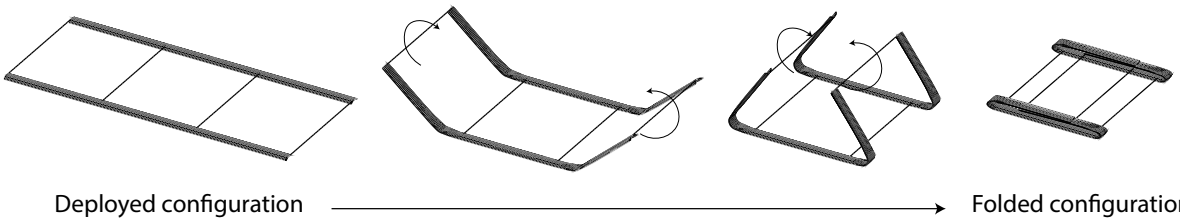

Fig. 1 Packaging scheme for strip with foldable longerons.

The experimental part of the study involved the design and construction of high quality test articles, as well as the development of a suspension system with low inertia and friction, and robust against changes of the strip geometry that might occur due to the propagation of the elastic folds. 3D Digital Image Correlation (DIC) was used to characterize the deployment with high speed cameras, and an algorithm to identify the elastic folds and track their propagation from DIC images was developed. The influence of air on the dynamic deployment of the strips was investigated by performing deployment experiments both in air and in vacuum. The effects of a thin film attached to the longerons and representing, for example, the photovoltaic cells and the electric substrate of a solar array, were also studied.

The computational part of the study used a high-fidelity finite element model of the strip to capture the elastic, localized deformation that occurs during the initial folding of the strip, the self-contact between different parts of the structure as the folding develops, and the strain energy stored during the folding process. It also captured the deployment dynamics and self-latching of the structure, and the effects of air on the deployment process. This part of the study builds on previous studies of the folding and deployment of tape springs [11] and tubular thin shells with longitudinal cutouts [12].

The paper is organized as follows. Section II describes the geometry of the strips and the suspension system. Section III discusses the implementation and characterization of the experimental setup. Section IV presents the experimental results. Section V describes the finite element model of the strip, discussing the simulation technique and the simulation parameters. Section VI presents the results from the simulations and compares them with the experiments. Finally, Section VII discusses the results and concludes the paper.

II. Description of Test Configuration

The basic architecture of the strip was derived from the Caltech Space Solar Power Project, described in previous publications [9, 13]. In the present study, the overall shape of the strip was simplified to a rectangle, to create a plane of symmetry that would allow a more symmetric deployment.

A. Strip Design

Figure 2 shows a strip consisting of two thin shell longitudinal elements, herein called "longerons", which provide bending stiffness to the deployed strip, and can be folded by forming elastic folds. They have an open cross section consisting of two circular arc flanges, connected by a flat web. This cross section design, first introduced in the Triangular Rollable And Collapsible (TRAC) booms [14], is symmetric with the respect to the axis of bending of the strip, and hence the moment-rotation relationship is independent of the sign of the moment. The longerons are connected by transverse rods, called "battens", which have a rectangular cross section and are responsible for the bending stiffness of the strip in the transverse direction, as well as for coupling the deformation of the longerons. The structure formed by the longerons and battens supports a thin film that in an actual application would be covered with functional elements, such as solar cells or RF antennas. The strip is terminated by two rigid connectors mounted in the middle of the outermost battens.

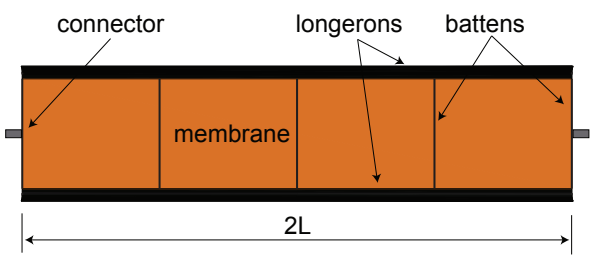

(a) Top view

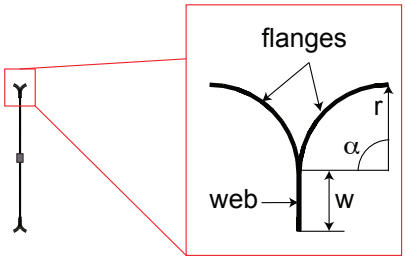

(b) Side view and detail of longeron cross-section

Fig. 2 Strip geometry.

B. Suspension System

Testing the deployment of thin-shell deployable structures in the presence of gravity is challenging, due to existence of low stiffness deformation modes in the folded configurations. Although gravity-related loads are rather small, due to the lightness of these structures, they can have a significant impact on deployment, and in fact many of these structures are unable to fully deploy under gravity unless they are properly supported throughout the deployment process.

Therefore, deployment testing of lightweight structures has involved drop towers [15, 16] or parabolic flights [17] [18] to achieve micro-gravity for a few tens of seconds. In most cases the deployable structures are supported for

deployment by suspension systems consisting of vertical cords attached to sliders following the structure or fly beams [19–21], but inertia and friction can significantly affect the deployment.

The chosen suspension system and the parameters required to fully define a deployment experiment are shown in Fig. !3. Since the present study has focused on 1 m scale strips, the distance between the pulleys was set at L_f = 1300 mm, to provide enough clearance for the structure during deployment.

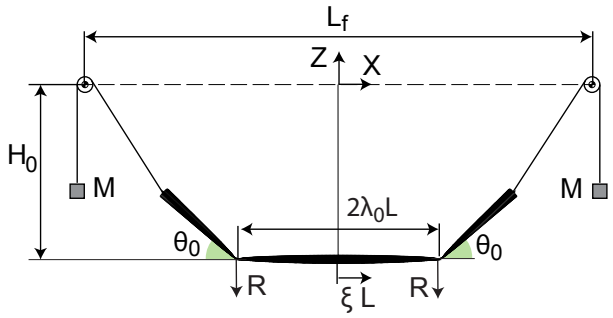

Fig. 3 Geometry and design parameters of suspension system.

When the strip is in the folded configuration, the two forces denoted by R in Fig. 3 are applied to the structure. These constraint forces are provided by a release mechanism that is instantaneously released to initiate deployment.

The folded configuration of the strip is defined by the position and angle of the elastic folds. For initially symmetric configurations of the folded structure, the initial geometry is defined by the distance between the folds $2\lambda_0 L$, with $\lambda_0 \in [0, 1]$ (where $\lambda_0 = 0$ corresponds to a single fold at the center of the strip), and the angle of the folds θ_0, here it should be noted that $\theta_0 = 0°$ corresponds to a fully deployed strip, whereas $\theta_0 = 180°$ would correspond to a fully tri-folded strip, although tightly packaged configurations are not compatible with the chosen suspension system and were not investigated. λ_0 was set by the position of the release system, whereas θ_0 was not controlled directly, but was controlled by the distance H_0 between the center of the strip and the pulleys, as shown in Fig. 3, and the mass M of the counterweights.

Initial experiments were carried out for initial heights $H_0 \in$ [250 mm, 750 mm] and masses $M \in$ [20 g, 100 g], corresponding to a range of fold angles between 10° and 60°. After exploring the parameter space defined by λ_0, H_0 and M in the range defined above, it was observed that the qualitative behavior of the strip during deployment does not vary significantly. Hence, only one specific set of parameters (H_0 = 400 mm, M = 50 g, λ_0 = 0.45), corresponding to an intermediate point of the parameter space, and representative of the behavior for a wide range of initial conditions, is considered in this paper.

III. Experimental Setup

A. Strip Prototypes

Two strip prototypes based on the architecture presented in Fig. 2 were manufactured, one with and one without the membrane. Both prototypes had the same nominal length $2L = 1125$ mm. The longerons had nominal flange radius $r = 12.4$ mm, flange opening angle $\alpha = 90°$, and web width $w = 8$ mm. They were connected by five, 200 mm long battens at equally spacing.

The flanges were manufactured from ultra-thin composite prepregs. The stacking sequence was $[\pm 45_{GFPW}/0_{CF}/\pm 45_{CFPW}]$, where GFPW represents a layer of Glass Fiber Plain Weave (25 gsm) scrim, and CF denotes a layer of unidirectional MR70 carbon fiber (30 gsm). An additional $[\pm 45_{GFPW}]$ bonding layer was interposed between the flanges in the web region. All layers were pre-impregnated with North Thin Ply Technology 380 CE cyanate ester resin. This laminate design has been previously shown to induce low stress concentration during coiling of the longerons [22] and its stiffness properties have been characterized [23].

The battens consist of pultruded carbon fiber rods with a 3 mm × 0.6 mm rectangular cross section, obtained from The Composite Store, Inc. They are connected to the webs of the longerons by Ω-shaped sleeves made of 2-ply JPS 1067 glass fiber composites with PATZ-F4A resin. The strips are attached to PTFE-coated glass fiber cords through 3D-printed plastic connectors, bonded to the center of the terminal battens.

The two strip prototypes nominally differ only for the presence of a 50 μm-thick Kapton membrane bonded to the web of the longerons of one of the prototypes. The geometry of each strip was measured with a FaroArm laser scanner. The actual radius and opening angle of the longerons, computed from the point cloud generated by the FaroArm, are reported in Table 1.

Strip type	Flange radius r [mm]	Flange angle α [°]	Total mass [g]
Strip 1, without membrane	12.4 ± 0.7	91.2 ± 4.6	23
Strip 2, with membrane	13.1 ± 1.1	80.3 ± 3.2	46

Table 1 Geometry and mass of strip prototypes.

B. Strip Moment-Rotation Relationship

The moment-rotation relationship for the elastic folds is of great importance, as it drives the self-deployment of the structure. It was measured with a large-rotation bending apparatus consisting of two sliders mounted in orthogonal directions [24] that measures the bending moments at the ends of the test sample as a function of a single applied rotation, during quasi-static unfolding of a strip with an elastic fold, Fig. 4. One of the sliders can freely translate along and rotate around the y-axis, but rotations around the z-axis (bending axis) are not allowed. The other slider can translate along and rotate around the x-axis; its rotation around the z-axis is controlled by a brushless DC motor.

Each slider is equipped with New Way air bearings (25.4 mm diameter, 90 psi operating pressure). Mini40 force/torque sensors by ATI Industrial Automation are attached to both sliders and measure all force and moment components applied by the structure, with a force resolution of 0.2 N and a torque resolution of 0.25 Nmm.

The strip was attached to acrylic clamps (grey in the figure) spaced 400 mm which were connected to the sliders. Because folds near a batten are energetically unfavorable and carry larger moments, the clamps were not symmetrically located with respect to the ends of the strip, to avoid forming a fold close to the central batten.

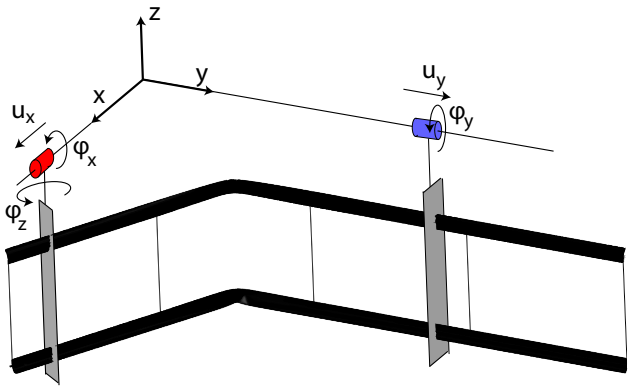

Fig. 4 Schematic of setup for strip bending tests.

To carry out a test, the strip was initially folded to an angle of 35° by manually forming an elastic fold at the center. Then, a rotation in the opposite sense to the folding direction was applied in small increments, until the strip had fully deployed. The results are reported in Fig. 5. Each test was repeated 3 times, showing a consistent behavior, with rms error of about 2 Nmm for both strips. The maximum variation of the peak moment was 23 Nmm for the strip without membrane, and 14 Nmm for the strip with membrane, corresponding to respectively 6% and 13% of the peak values.

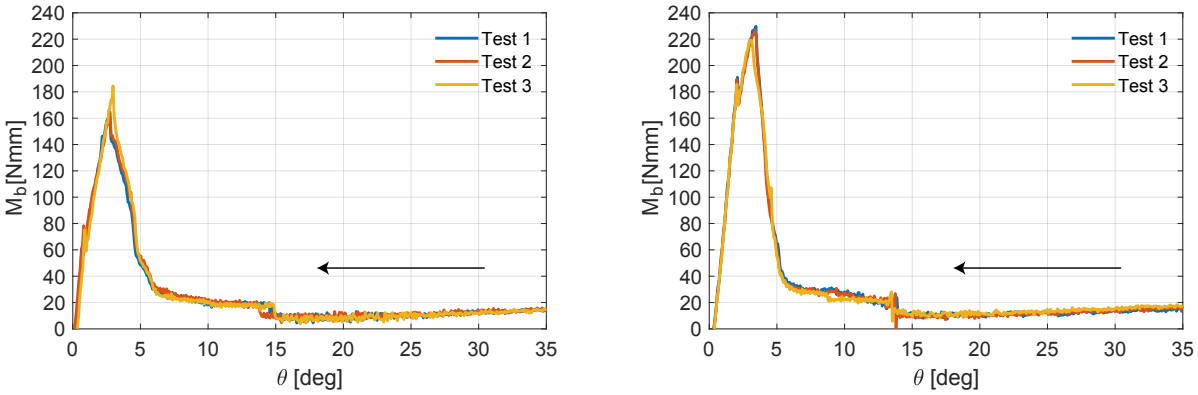

(a) Strip without membrane

(b) Strip with membrane

Fig. 5 Moment-rotation relation for strip prototypes.

It was observed that during unfolding the fold undergoes shape and position changes. Specifically, for angles greater than 15°, the fold remains symmetric and the bending moment is mostly constant, slightly decreasing with the angle. At approximately θ =15°, the bending moment suddenly increases while the shape of the fold switches from a symmetric to an asymmetric configuration. For smaller values of θ, the moment keeps increasing until it reaches a peak for $\theta \approx 3°$, after which the fold disappears as a local buckle forms in the longeron flange that is under compression.

Both strips exhibited similar qualitative behavior, although some quantitative differences were noted. For $\theta > 15°$, the bending moment in the strip without membrane was about 15% higher than for the strip with the membrane, due to the larger flange angle of this strip, see Table 1. The strip with the membrane had 30% higher peak moment, due to the fact that the folds in the two longerons disappear at the same time, unlike the strip without the membrane. Quasi-static unfolding simulations, presented in Sec. VI.A, show that the loss of symmetry in the disappearance of the elastic folds in the two longerons significantly decreases the overall peak moment. The reduction in the moment is smaller for the strip with the membrane, suggesting that the coupling between longerons introduced by the membrane makes the behavior of this strip closer to the ideal case.

C. Experimental Apparatus

This subsection describes the experimental setup for the strip deployment experiments. It features a suspension system to support the weight of the strip during deployment, a release mechanism to hold the strip in its initial, folded configuration, and a metrology system to capture the deployment with high spatial and time resolution. The test structure and experimental apparatus are shown in Fig. 6.

(a) Setup with metrology system.

(b) Detail of pulley.

(c) Detail of release mechanism.

Fig. 6 Apparatus for strip deployment tests.

The suspension system included two 12.4 mm diameter, nylon miniature pulleys mounted on ball bearings (SP4088 from Carl Stahl Sava Industries). The pulleys were installed on a support structure consisting of aluminum T-slotted frames. PTFE-coated glass fiber cords run over the pulleys and were connected to the strip at one end and to weights at the other end. By varying the height of the pulleys from the ground and the mass of the weights, the initial fold angle of the strip could be adjusted. For the experiments described in this paper, the height of the pulleys and the mass of the weights were chosen such that the initial fold angle would be approximately 45°, as previously discussed in Sec. II.B. It was shown by analysis that the inertia of the pulleys contributes to less than 1% of the total inertia of the system, and hence its effect was considered negligible. The analytical model suggested that friction in the ball bearings can significantly affect the dynamics of the suspension system, and therefore a detailed characterization of the friction of the system was performed, as discussed next.

The release mechanism was responsible for holding the strip in the folded configuration and releasing it upon a deployment command. The release actuation was provided by two R12X12 DC pull-type linear actuators (24 V, 2.5 W) from Magnet-Schultz of America. These actuators consist of solenoids that pull a central magnetic shaft upon powering. They were connected in parallel to a power supply, in order to achieve synchronized release, within 2 ms. The strip was connected to the release actuators by cords with negligible mass. Specifically, two cords across the strip were attached to the webs of the longerons and their location along the strip defined the initial position of the elastic folds. A cord loop placed across the centers of the cords and the shaft of the corresponding release actuator was held taut by the counterweights of the suspension system. By retracting the shafts of the actuators, the cord loops were released and the deployment was initiated.

Lastly, the metrology system consisted of two Photron UX100 monochrome high speed cameras set at a frame rate of 500 fps. The system was configured to provide a 1.2 m field of view with 500 mm depth of field. A 72,000 lumens REL Sure Bright light module with 120 white LEDs completed the setup. A speckle pattern was applied to the top face of the longerons, with approximate speckle size of 5 mm, to perform DIC on the image pairs obtained during each test. Photogrammetry was used to extract the coordinates of several targets placed on both the strip and the aluminum frame, which were used to define a global coordinate system for the experiment. Both DIC and photogrammetry measurements were performed using the VIC-3D software by Correlated Solutions.

The experimental setup described above was used to perform deployment tests both in air and in vacuum. The tests in vacuum were performed in an altitude chamber with internal volume of 2.4 m $\times$ 2.4 m $\times$ 2.4 m, at NTS Santa Clarita, CA. During these experiments, the pressure was maintained at 55 torr (corresponding to about 7% of standard atmospheric pressure). The temperature within the chamber, which was not actively controlled, varied between 20°C and 30°C.

D. Suspension System Characterization

The friction torque in the pulley bearings of the suspension system was measured experimentally. The experimental setup consisted of two masses $M_1 \neq M_2$ attached to the opposite ends of a cord running on a pulley, as shown in Fig. 7. The masses were initially held stationary, and started moving vertically when they were released, with the heavier one accelerating downwards. A target placed on the heavier mass was tracked using the high speed camera system, which acquired images at 500 fps. Photogrammetry was performed with VIC3D to extract the coordinates of the target. From the measured vertical coordinates, the variation of the target height, h, was obtained as a function of time and a 2^{nd} order polynomial of the form $h(t) = c_2t^2 + c_1t + c_0$ was fitted to these data to estimate the acceleration of the mass:

$$\ddot{h} = 2c_2 \tag{1}$$

Each experiment was repeated 3 times, and the measured accelerations were repeatable within 1.5% of their mean value.

The pulley friction torque was obtained from the equation of motion:

$$(M_1 - M_2)gR - T_f = \left[I_p + (M_1 + M_2)R^2\right] \frac{\ddot{h}}{R} \tag{2}$$

where R and I_p are the radius and the second moment of inertia of the pulley, respectively, and T_f is the friction torque on the pulley. Solving for T_f, substituting $\ddot{\beta} = \ddot{h}/R$, and using $\ddot{h}$ from Eq. 1 gives:

$$T_f = (M_1 - M_2)gR - \left[I_p + (M_1 + M_2)R^2\right] \ddot{\beta} \tag{3}$$

T_f was computed for nine different combinations of M_1 and M_2 in the range [15 g,... 100 g].

Given the relatively low angular velocity of the pulley during a deployment experiment, it is reasonable to neglect viscous effects in the pulley ball bearing, and to assume that friction is entirely due to the elastic rolling resistance [25], which increases linearly with the normal load on the bearing. Therefore, the normal force F_n is given by:

$$F_n = (M_1 + M_2)g - (M_2 - M_1)\ddot{\beta}R \tag{4}$$

where the first term on the right hand side describes the static contribution from the weight of the two masses, whereas the second term captures the inertial effects. This equation indicates that the friction torque depends on both the sum $M_1 + M_2$ and the difference $M_2 - M_1$ of the two masses.

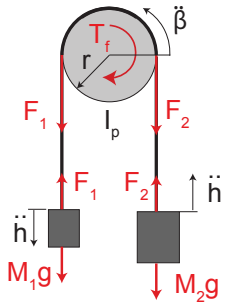

Fig. 7 Characterization of pulley friction torque.

IV. Experimental Results

Deployment experiments were performed with the two strip prototypes, both in air and in vacuum. Each experiment was repeated three times and the results of repeated tests were consistent. Figure 8 shows snapshots from the deployment in vacuum of the strip with membrane, starting from the folded configuration, with $H_0 = 400$ mm. The strip maintained its initial symmetry until the end of deployment, with the elastic folds remaining stationary and opening out monotonically. At $t = 300$ ms, symmetry was lost as one of the elastic folds (on the right hand side) latched before the other fold. After both folds had latched, the strip began to vibrate in a small-amplitude, smoothly curved mode.

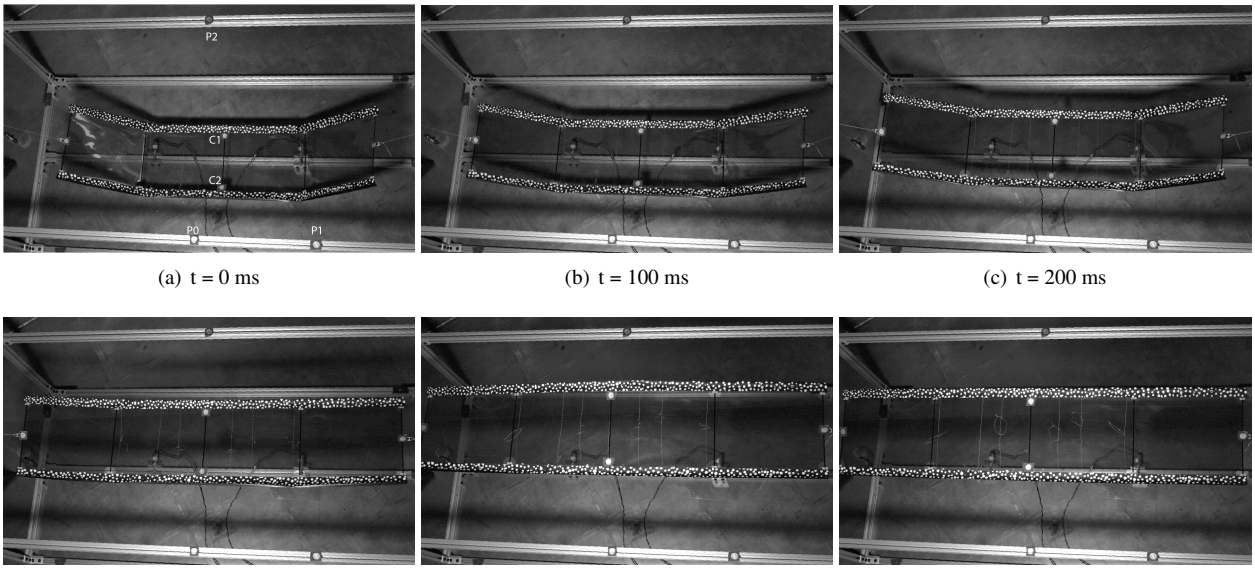

(a) t = 0 ms (b) t = 100 ms (c) t = 200 ms

(d) t = 300 ms (e) t = 400 ms (f) t = 500 ms

Fig. 8 Snapshots from deployment of strip with membrane, in vacuum. See also the supplemental video S1.

The images captured by the high speed cameras were processed with VIC-3D, which provided a point cloud for each longeron, at each frame. An algorithm was developed in MATLAB to identify and track the elastic folds and also measure the fold angles. The algorithm consists of an initialization phase, which is run on the first image taken during

the experiment, and a loop, performed on all subsequent frames. The initialization consists of the following steps:

1) Definition of global coordinate frame. The coordinates of 3 targets located on the aluminum frame (P_0, P_1 and P_2 in Fig. 8(a)) are extracted with photogrammetry and are used to define a global coordinate system consistent with Fig. 3.
2) 2D projection. The point clouds are projected on the x-z plane (see Fig. 3) for increasing values of x.
3) Definition of curvilinear abscissa. The centerline of each longeron is obtained by computing the median of the coordinates of a 50-point moving window (Fig. 9). From a statistical perspective, the median is more robust than the mean to outliers in noisy data [26] and therefore median filters are often used in combination with DIC [28]. A curvilinear abscissa $s = \xi L$ (Fig. 3) is defined on the centerline, using $s_i = s_{i-1} + \Delta s_i$, for $i = 2, ...N_p$. Here, Δs_i is the distance between 2 consecutive points on the centerline and N_p is the total number of points. The origin of the abscissa s is defined at the center of the strip. A value of s is then assigned to each point in the cloud, by projecting it on the centerline of the longeron and interpolating the previously computed values of s on the centerline. Note that the curvilinear abscissa defines a body-fixed frame, which identifies each point in the cloud, throughout deployment.
4) Computation of local tangent. The local tangent $\mathbf{T}(s)$ to each longeron is computed with a Principal Component Analysis (PCA) on a 50-point moving window from the point cloud [27]. By performing an eigenvalue analysis on the covariance matrix of the coordinates of the points in the moving window, this algorithm returns the directions along which the points are distributed. The Principal Component is associated with the largest variance and identifies, in this case, the local tangent to the longeron. PCA is used to filter the noise due to some of the points being on the web and others on the flange of the longerons, resulting in a more robust algorithm. Each local tangent is associated with a value of the curvilinear abscissa that corresponds to the median of the abscissas of the points in the moving window. By computing the dot product of the local tangents with the global x-axis, the local angle $\theta(s)$ of the longeron as a function of s is obtained.
5) Identification of folds. The longitudinal curvature $\kappa(s)$ of each longeron is computed from $\kappa(s) = \|\frac{d\mathbf{T}(s)}{ds}\|$, where the derivative is computed numerically using a symmetric finite difference scheme. The resulting curvature is first smoothed using a 50-point moving average, Fig. 9. The two highest peaks in the $\kappa(s)$ curve define the initial location of the elastic folds.

Once this initialization has been completed, the algorithm iterates over each frame, repeating only steps 4) and 5). To track the localized folds, the search for the peaks in longitudinal curvature is performed in a ± 20 mm region centered at the location of the folds from the previous frame. In this way, the folds can be tracked even when their longitudinal curvature becomes small, towards the end of deployment, and hard to distinguish from the noise floor.

The outcome of the above-described algorithm is a map showing the distribution of slope and curvature along each longeron, as a function of time. An example is shown in Fig. 10 for the deployment in air of the strip without membrane.

The curvilinear abscissa on the y-axis is non-dimensionalized with respect to the length of the strip using $\xi = \frac{s}{L}$, so that $\xi \in [-1, 1]$, with $\xi = 0$ being at the center of the strip. The results for the two longerons are very similar and therefore only one map has been shown.

Figure 10(a) shows that in each longeron there are three distinct regions with uniform slope. Specifically, the central region is approximately horizontal, whereas the other two regions have equal and opposite slope, decreasing over time until the strip has fully deployed. Figure 10(b) shows two well-defined curvature peaks, corresponding to the location of the elastic folds, which remain stationary during deployment. Although these maps provide a full-field characterization of the deployment process, in the rest of this paper the results are presented in terms of the angle of the folds and the height of the center of the strip vs. time. These plots provide insights into the dynamics of the elastic folds, as well as the rigid body translation of the structure. The angle of each fold is computed by taking the median of $\theta(s)$ between the location of the fold and the end of strip, at each time increment. The height of the center of the strip is provided by the z coordinate of two targets placed next to the center of each longeron (C_1 and C_2 in Fig. 8(a)). The results for each experiment are shown in the rest of this section.

Figure 11(a) shows plots of the angle of the elastic folds as a function of time, for the strip without membrane. Since each longeron has two folds, the plot contains two lines starting from equal and opposite angles. Solid, dashed and dotted lines correspond to different runs of the same experiment. Also, green and blue lines correspond to the tests in air, whereas orange and red lines correspond to the tests in vacuum. Using this plot, the deployment time can be defined as the time when all fold angles become zero for the first time.

Overall, the tests are symmetric, with both longerons undergoing the same angle variation on both folds. The fold angle starts from approximately ±42°, and then decreases until becoming zero at about $t = 300$ ms. During deployment, an oscillation of the fold angle, with a period of about 220 ms, can be observed. After reaching $\theta \approx 0°$, the localized folds disappear, and the strip vibrates with small-amplitude deformations.

Comparing the tests in vacuum and in air, it can be observed that there is almost no difference, indicating that the

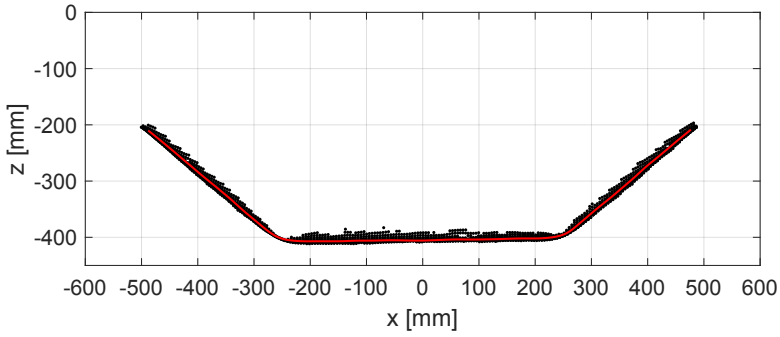

Fig. 9 Point cloud projected on x-z plane and longeron centerline (in red). Data from deployment test in air of strip without membrane.

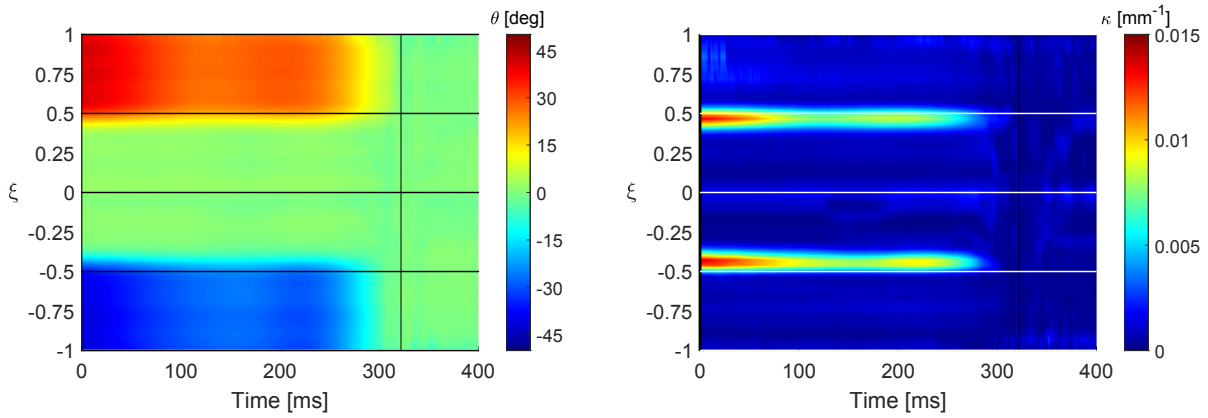

(a) Map of local slope

(b) Map of longitudinal curvature

Fig. 10 Time variation of slope and longitudinal curvature for strip without membrane deploying in air. Results are shown for one longeron only.

effects of added air mass and air drag on the unfolding process of a strip without membrane are negligible. The plot in Fig. 11(b) shows the height of the center of the strip during deployment (with the zero corresponding to the height of the pulleys). The plot shows that the height increases monotonically until the strip is fully deployed at $t = 300$ ms. Afterwards, the structure continues to move upwards as a rigid body and it overshoots $H = 0$, reaching a maximum height at $t = 400$ ms. The longerons maintain the same height during deployment, indicating that there is no twisting of the strip. In this case, comparing the experiments in air and in vacuum, it can be noticed that the latter is faster during the last portion of deployment (after $t = 250$ ms), and it reaches a higher peak at approximately the same time.

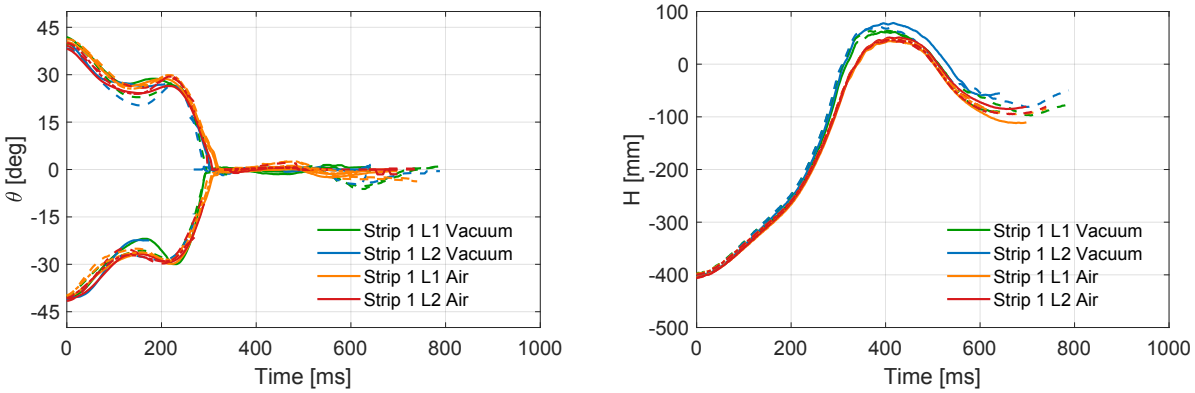

(a) Fold angle.

(b) Height of strip center.

Fig. 11 Test results for strip without membrane. Solid, dashed and dotted lines correspond to different runs of the same experiment. L_i denotes longeron i.

Figure 12 presents the results for the strip with membrane, both in air and in vacuum. Again, the behavior of the strip is symmetric and the three runs of the experiment are consistent. However, for this strip the presence of air plays a significant role, with the deployment in air being about 1.7 times slower than in vacuum (750 ms vs. 450 ms). Similarly

to the strip without membrane, the fold angle oscillates during deployment, with an average period of 280 ms in air vs. 220 ms in vacuum. Also, the amplitude of the oscillation is smaller for deployment in air than in vacuum. Figure 12(b) shows the height of the center of the longerons over time. For deployment in air, the strip reaches its final height after 950 ms, never overshooting the vertical location of the pulleys. For deployment in vacuum, the vertical motion is much faster and the maximum height is reached after 550 ms.

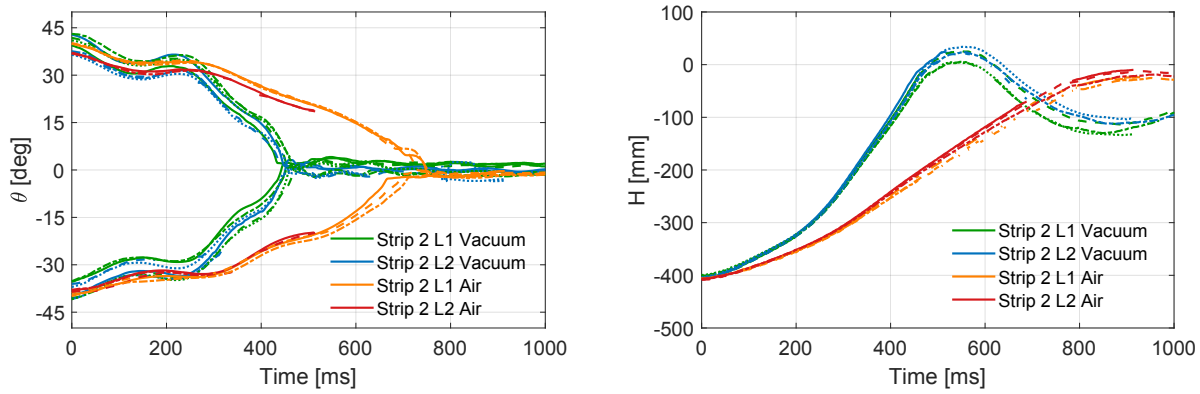

(a) Fold angle.

(b) Height of strip center.

Fig. 12 Deployment results for strip with membrane, tested in air and vacuum. Solid, dashed and dotted lines correspond to different runs of the same experiment.

In summary, the experiments have shown that, for the suspension system concept studied in this paper (and for the chosen values of H_0 and M), the elastic folds do not move and essentially behave as fixed, self-latching elastic hinges that deploy in a consistent and repeatable fashion. If the structure is folded in a symmetric way, symmetry is also preserved throughout the deployment.

V. Numerical Model

Numerical simulations of the packaging and deployment of the strip were carried out with the Simulia Abaqus/Explicit 2020 finite element software. The Abaqus model is shown in Fig. 13. Fig. 13(a) describes the overall geometry of the model, and Fig. 13(b) shows a schematic representation of the suspension system model, which is discussed in detail in Sec. V.B. The longerons were modeled with S4R reduced-integration shell elements, and their material properties were directly defined by the ABD matrix for the flanges and the web, based on previous measurements on coupons of a similar laminate [23]. The battens were modeled with B31 linear beam elements. The Ω-shaped connectors between the longerons and the battens were assumed rigid and were modeled with kinematic coupling constraints between the end nodes of the battens and a region of the longeron web of the same size as the physical connector. The suspension system was modeled using a combination of one-dimensional connector elements. More details about this model are provided later in this section. The membrane was attached to the webs of the longerons and to the battens using tie constraints.

A uniform mesh of approximately 2 mm × 2 mm was used for all parts of the model. Based on the essentially symmetric deployment observed in the experiments, symmetry about the mid-plane of the strip was assumed, thus reducing the total number of elements by a factor of two. The resulting model contained 81,355 nodes and 79,556 elements, i.e. 24,156 shell elements and 54,900 membrane elements.

The large number of elements in the model is required to accurately model the thin shell longerons and the wrinkled regions in the membrane. Resolving the deformation and stress distribution near a fold requires multiple elements across the longeron cross-section. The shell element size was chosen based on the convergence of the steady-state moment during the quasi-static strip bending experiments described in Sec. VI.A.

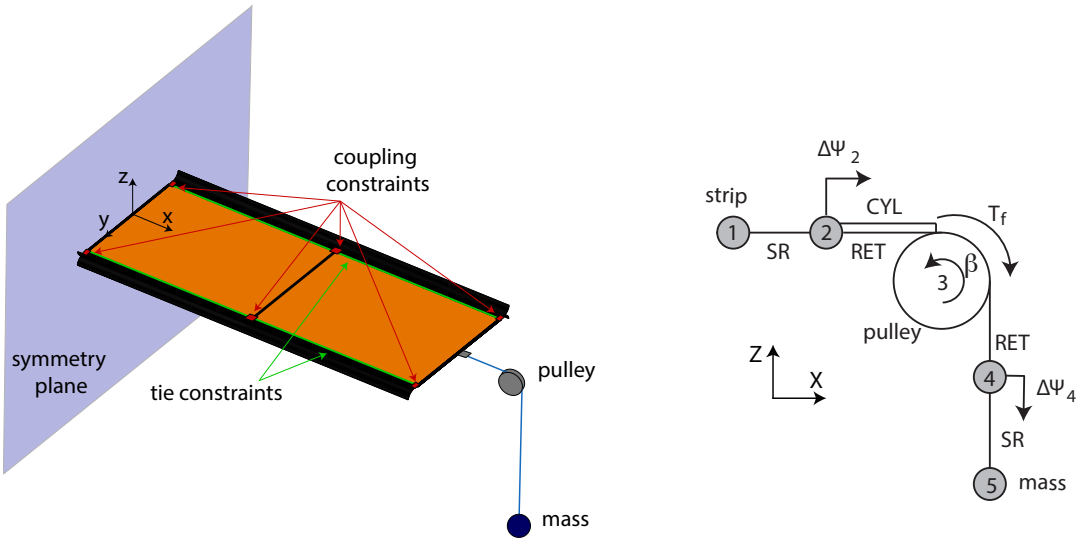

(a) Model of symmetric strip.

(b) Suspension system model.

Fig. 13 Finite element model of strip with membrane.

A. Membrane Model

The membrane was modeled with M3D4R reduced integration membrane elements and wrinkling was captured with the Iterative Material Model (IMP) [29, 30]. This model is based on a mixed stress/strain criterion to identify three regimes for the membrane (slack, wrinkled and taut) where each regime is associated with a different material tangent stiffness matrix. For a taut membrane, the constitutive relation is based on the standard stiffness matrix $\mathbf{D_t}$ for an isotropic membrane. A slack state corresponds to no stress in the membrane, hence the stiffness matrix $\mathbf{D_s}$ is null. Finally, for a wrinkled membrane, an effective stiffness matrix $\mathbf{D_w}$ is defined, based on the assumption that the wrinkles are aligned with the direction of principal stress in the membrane, and that the stress is zero in the direction normal to

the wrinkles. Hence, the resulting model is expressed as:

$$\mathbf{D_s} = \mathbf{0} \tag{5a}$$

$$\mathbf{D_w} = \frac{E}{2}\begin{bmatrix} 2(1+P) & 0 & Q \\ 0 & 2(1-P) & Q \\ Q & Q & 1 \end{bmatrix} \tag{5b}$$

$$\mathbf{D_t} = \frac{E}{1-\nu^2}\begin{bmatrix} 1 & \nu & 0 \\ \nu & 1 & 0 \\ 0 & 0 & (1+\nu)/2 \end{bmatrix} \tag{5c}$$

where E, ν are the elastic modulus and Poisson's ratio of the membrane. The parameters P and Q are defined as:

$$P = \frac{\epsilon_x - \epsilon_y}{\epsilon_1 - \epsilon_2} \tag{6a}$$

$$Q = \frac{\gamma_{xy}}{\epsilon_1 - \epsilon_2} \tag{6b}$$

where ϵ_x, ϵ_y are the Cauchy strains in the x, y coordinates and ϵ_1, ϵ_2 are the principal strains.

Various implementations of the IMP algorithm have been successfully used in finite element codes, both with implicit [31] and explicit [32] integration schemes. The particular implementation that was used in the present study was the Abaqus/Explicit VUMAT subroutine in Ref. [32].

B. Suspension System Model

Models for cables and pulleys have been developed in the context of cranes, electrical transmission lines and seat belts. Electrical transmission lines loaded by self-weight have been modeled as truss elements with zero-sized frictionless pulley allowed to slide [33]. A formulation that accounts for friction between cords and pulleys in cranes [34] allows for different tensions in the cord segments on the two sides of the pulley, but does not consider inertial effects on the pulley.

With this background, the chosen model was based on seat belt systems models for dynamic simulations of automotive crash events [35, 36], which use combinations of slip rings and retractor elements. Slip rings are 2-node elements that enable a "material flow" degree of freedom, which allows mass to enter or exit the element, and hence to increase or reduce the element's length without elastic deformation. Connecting two slip rings in series, the mass exiting from one element enters the other element through their shared node. Retractor elements, instead, convert the material flow at one node into rotation of the other node. Both of these elements are available in Abaqus/Explicit. It

should be noted that a five node model for the suspension system is the minimum number of connectors required to capture the physics of the problem, i.e., including the inertia and friction in the pulleys, as well as the variation of the cord tension due to the inertia of the end masses.

A schematic model of a suspension pulley is shown in Fig. 13(b), where the circles 1-5 represent the nodes of the connector elements. Node 1 corresponds to the strip-cord connector and is connected to the central nodes of the strip's outermost batten using MPC beam constraints. Node 3 represents the pulley, which has only one rotational degree of freedom, about the y-axis. Node 5 represents the counterweight attached to the end of the cord, whereas nodes 2 and 4 are auxiliary intermediate nodes. Slip ring (SR) elements model the cords, connecting nodes 1-2 and 4-5. To prevent the cords from experiencing axial compression during dynamic loading, a bi-linear elastic model is assigned to the slip rings, with tensile stiffness $K_t = 1000$ N/mm and compressive stiffness $K_c = 1$ N/mm. These values were chosen through a sensitivity study which showed that, under the expected loads, the simulations were stable and the cords effectively behaved as rigid in tension and slack in compression.

To take into account the inertial effects of the pulley, retractor elements (RET) between 2-3 and 4-3 convert the material flow at nodes 2 and 4 into rotation of node 3, according to:

$$\beta = \frac{\Delta\Psi_2}{R} = \frac{\Delta\Psi_4}{R} \tag{7}$$

where R is the radius of the pulley and $\Delta\Psi_2$, $\Delta\Psi_4$ define the material flow at nodes 2 and 4. Note that $\Delta\Psi_2 = \Delta\Psi_4$ because the retractor elements are connected in series.

Lastly, friction in the pulley bearing was captured by adding a second connector element between nodes 2 and 3, in parallel with the retractor element. This element models a cylindrical joint (CYL) that constrains all relative displacements between its nodes, except for the relative rotation about the y-axis. It provides the friction torque associated with the rotational degree of freedom, β, through the relationship:

$$T_3 = -\text{sign}(\beta) T_f \tag{8}$$

where T_f is a constant obtained from the experimental characterization of the suspension system described in Sec. III.D.

The experiment presented in Sec. III.D was used as a benchmark to validate the above-described model of the suspension system and to determine the pulley friction. The numerical model agreed with the analytical solution from Eq. 2 and with the experiment with less than 0.1% and 1% error, respectively.

The suspension system model described in this section was used for all the simulations, except for the quasi-static unfolding test in Fig. 16, which did not require a suspension system because it was supported by the setup described in Fig. 4.

C. Air Model

Modeling the effect of air on the deployment dynamics of lightweight large-area structures in a general way would require a coupled fluid-structure model [38] which would have been beyond the scope of the present study. The approach that was adopted was based on existing models for the vibration of large membranes. Membranes vibrating in air have lower natural frequencies and higher damping than in vacuum [37] and for simple geometries it can be shown that the effect of air pressure in the equations of motion can be described in terms of a frequency-dependent added mass and a radiation damping term [38].

A simple vibration model [39] used a geometric argument to define an effective air volume, based on the velocity field for any chosen vibration mode, and defined a non-uniform added air mass that is maximum at the center of the membrane and zero at the edges. Higher fidelity models have been developed to explicitly include the air around the membrane, either using the boundary element method [40] or defining an air box with finite elements [38].

Hence, it was assumed that a half-cylindrical volume around the strip is forced to move with the structure. The height of the added-air volume above the structure only varies with the transverse coordinate, and is given by:

$$z_a(y) = \sqrt{\left(\frac{W}{2}\right)^2 - y^2} \tag{9}$$

where W is the width of the strip. The corresponding mass of air added to the structure is therefore:

$$m_a = 2\rho_a L \int_{-\frac{W}{2}}^{\frac{W}{2}} z(y)dy = \frac{\pi \rho_a W^2 L}{4} \tag{10}$$

where $\rho_a = 1.225\ kg/m^3$ is the standard air density.

The added air mass was uniformly distributed over the area of the Kapton membrane by scaling the mass of the membrane with the factor:

$$k = \frac{m_0 + m_a}{m_0} \tag{11}$$

where m_0 is the mass of the membrane and m_a the air mass.

From an implementation standpoint, the added air mass could be introduced by increasing the density of the membrane. However, this would increase not only the inertia of the structure during deployment, but also its gravity loading, thus altering the obtained folded configuration as well as the height of the structure in the fully deployed configuration. Therefore, the added air mass was introduced by using mass scaling, which is a technique often used in quasi-static problems with explicit solvers. Mass scaling has the advantage of increasing the density of the material and, therefore, the stable time increment of the solver, drastically reducing the number of increments needed to perform long simulations. The mass scaling formulation in Abaqus/Explicit only affects the inertial term in the equations of motion of the model, but the scaling coefficient is not included in the calculation of gravity loads. Therefore, it is ideal to model

the effect of air on the dynamics of the structure, without affecting its equilibrium configuration.

According to this model, the added air mass for the strip with membrane deploying in air was $m_a = 31.7$ g. The membrane mass $m_0 = 16$ g and the scaling factor $k = 3.0$. The added mass due to the residual air in the experiments in near-vacuum conditions, described in Section III.C, was 3.0 g and it was neglected.

For the strip without membrane, the air volume would consist of two half-cylinders with diameter equal to the width of the two longerons. The resulting added mass for deployment in air and near-vacuum conditions would have been 0.45 g and 0.04 g, respectively, and it was neglected.

The second aspect of the air-structure interaction, damping, can be simply expressed by a force D:

$$\frac{D}{A} = \frac{1}{2}\rho_a V_a^2 c_D \tag{12}$$

where ρ_a and V_a are the density and velocity of the undisturbed flow, A is the total area of the structure and c_D is the drag coefficient, which depends on the geometry of the body and the Reynolds number. For a half-cylinder with the concave side facing the flow $c_D \sim 2.3$ [41].

This air drag model was implemented in Abaqus/Explicit using a stagnation pressure load, defined as:

$$p_s = -c_s(\mathbf{v} \cdot \mathbf{n})^2 \tag{13}$$

where $\mathbf{v}$ is the velocity of the point on the surface where the load is applied, and $\mathbf{n}$ the local normal. Substituting $|\mathbf{v}| = -V_a$ and equating the right-hand sides of Eqns. 12-13 gives:

$$c_s = \frac{1}{2}\rho_a c_D \tag{14}$$

In conclusion, air effects were only considered for the deployment in air of the strip with membrane. They were modeled as an additional mass, defined by scaling the membrane with $k = 3.0$, and damping defined by a stagnation pressure with $c_s = 1.4087\ kg/m^3$.

D. Simulation Details

Simulations with the symmetric model shown in Fig. 13 were performed in Abaqus/Explicit 2020 and were organized in five steps, as described next.

1) In the first step, the suspension cords were tensioned by applying gravity. Localized folds were formed in the longerons by the application of equal and opposite pressures of 0.1 MPa distributed on both flanges, over a 20 mm long region. This length includes enough elements to avoid locking of the mesh induced by excessive shearing.

2) A rigid cylinder with radius equal to the flange radius was used to push the strip into its folded configuration, using displacement control.
3) The residual kinetic energy in the structure was allowed to dissipate to less than 1% of the maximum strain energy. At this point, the folded configuration was considered to have reached equilibrium.
4) In the deployment step, the cylinder was instantaneously removed and the structure was allowed to self-deploy.
5) A final equilibrium step was carried out, to dissipate the kinetic energy from deployment and obtain the final deployed configuration of the strip.

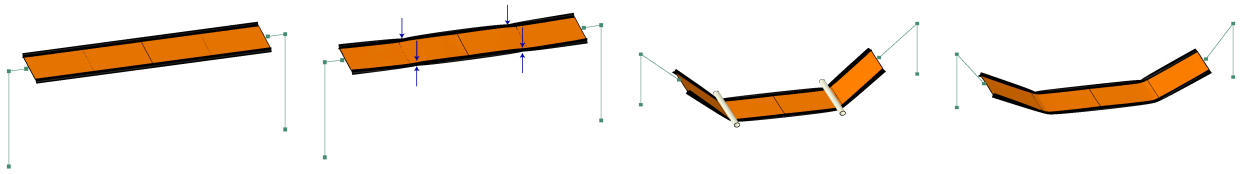

(a) Initial configuration (b) Localized folds (c) Folding (d) Deployment

Fig. 14 Simulation sequence (actual simulation only includes half of the strip).

Numerical damping was used to reduce unphysical, high frequency vibration that is characteristic effect of explicit simulations. Previous studies have shown that a velocity-dependent viscous pressure, defined as $p = -c_v \mathbf{v} \cdot \mathbf{n}$, is effective in dissipating such vibration in thin shell structures [12, 42]. Sensitivity studies of strip deployment have shown that a small amount of linear bulk viscosity, proportional to the volumetric strain of the finite elements, is also beneficial to prevent numerical instabilities, and hence a combination of both damping models was used. Table 2 presents the values of the main parameters for each of the above five simulation steps.

Step	Duration [s]	Linear bulk viscosity b_1	Viscous pressure coefficient c_v $[kg\ m^{-2}s^{-1}]$
1. Create folds	0.1	10^{-4}	10
2. Folding	0.5	10^{-4}	10
3. Equilibrium	0.26	10^{-4}	100
4. Deployment	0.8	10^{-8}	0
5. Equilibrium	0.3	10^{-4}	100

Table 2 Simulation parameters

The duration of the first three steps was chosen by trial and error, such that the correct folded configuration could be achieved in the shortest possible computational time. The duration of the deployment step was chosen to be longer than the actual deployment time of the strip (defined as the time at which the fold angles become zero for the first time). The duration of the final equilibrium step was chosen such as to allow sufficient dissipation of the end-of-deployment vibration and rigid body oscillation of the strip, using the previously chosen values of the numerical damping. With these settings, a complete simulation of packaging and deployment, using 8 CPUs on a server with 3.5 GHz Intel

Xeon Gold 6144 processor took about 83 hours 45 minutes (30 hours 20 minutes for folding, 53 hours 25 minutes for deployment) for a strip with membrane vs. 25 hours 25 minutes for a strip without membrane (17 hours 20 minutes for folding, 8 hours 5 minutes for deployment).

Figure 15 shows the energy contributions throughout the simulation of the strip with membrane, deploying in air. The black, dashed line indicates the total energy, defined in Abaqus as the sum of all the energy components in the model, minus the external work. It remains constant and approximately equal to zero throughout the simulation, confirming that there is practically no energy loss from the model. The artificial energy, associated with hourglassing modes in the finite element mesh, is very small throughout the simulation. The viscous dissipation increases during the folding process and is associated with the viscous pressure introduced during that step. In the deployment phase, it slightly grows due to the air drag. In the final equilibrium step, the viscous dissipation further increases as additional damping is introduced in the model (in the form of viscous pressure and bulk viscosity) to reach the final equilibrium state. Regarding the strain energy of the strip, the largest contribution comes from the formation of the elastic folds during pinching of the longerons, in the first step of the simulation. Additional strain energy is stored during folding, as the angle of the folds is increased. During the deployment step, the strain energy gradually decreases to 10% of its value in the folded configuration, when the elastic folds latch in the deployed configuration. The residual strain energy, associated with elastic vibration of the strip, is released in the final equilibrium step.

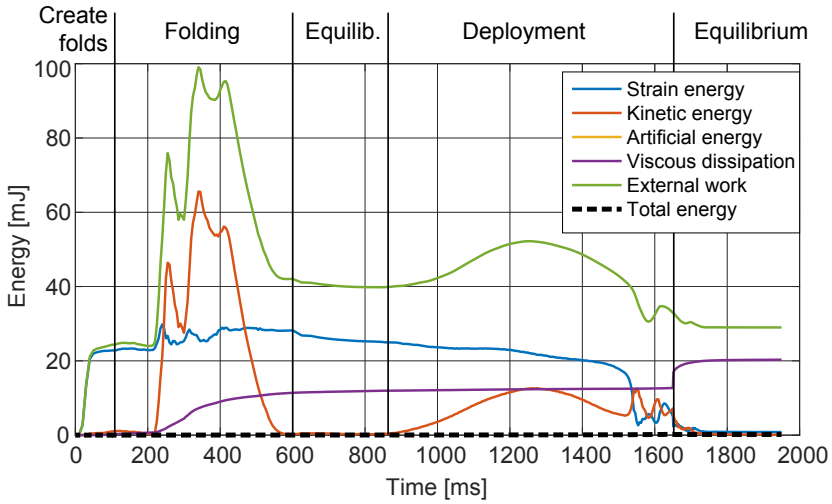

Fig. 15 Energy terms for strip with membrane deploying in air.

Note that the folding process is not quasi-static, since the kinetic energy is quite high compared to the strain energy, but is dissipated to less than 1% of the strain energy before deployment is initiated. The same approach was previously adopted in Ref. [12]. During deployment of the strip, the kinetic energy varies smoothly, reaching its maximum after 410 ms from the beginning of deployment (i.e., 1270 ms from the start of the simulation); then, it suddenly increases

when the elastic folds latch, and afterwards it oscillates. In the final equilibrium step, the residual kinetic energy is almost entirely dissipated.

VI. Comparison between Numerical Results and Experiments

The first part of this section validates the numerical model of Section V using the quasi-static unfolding of a strip as a benchmark problem. The second part presents a comparison between the experimentally measured deployment behavior of the strips, with and without membrane, with the corresponding numerical simulations.

A. Model Validation

A quasi-static simulation of the deployment of both strips was performed using Abaqus/Standard 2020, with boundary conditions that matched the experimental setup in Sec. III.B. In the first part of the simulation, localized folds were imposed by applying pressure on both flanges of the longerons (similarly to step 1 of Section V.D), and the strips were folded to an angle $\theta = -35°$, by controlling the end rotation. It was followed by a deployment step in which θ was decreased to zero.

The deployment simulation showed that the strip undergoes several instabilities, because the elastic folds tend to move along the longerons, which makes convergence difficult to achieve. A small amount of viscous stabilization was introduced to help the solver achieve equilibrium and an analysis of the sensitivity to this parameter showed that setting the maximum allowable ratio of stabilization energy to total strain energy equal to 10^{-7} provides sufficient stabilization with negligible effect on the predicted moment in the strip. However, stabilization up to 10^{-4} was required in the final part of deployment, when snapping of the elastic folds releases significant amounts of energy. The results are shown in Fig. 16.

Overall, the simulations are in good agreement with the experiments for large angles ($\theta > 10°$), correctly capturing the steady-state moment of the strip. For smaller θ the localized folds disappear and the simulations significantly overpredict the peak moment, which is over 2 times higher than the measured value for the strip without membrane, and 1.4 times higher for the strip with membrane.

There are two reasons for this discrepancy. First, as explained in Sec. III.B, the experiments show that the localized folds transition from a symmetric to an asymmetric configuration for $\theta \approx 15°$. At the peak moment, the localized folds turn into local buckles along the compression flanges. As $|\theta|$ is decreased, the buckle's amplitudes gradually decrease. The simulation misses this transition from symmetric to asymmetric folding, although it captures well the transition to local buckling of the compression flanges. Hence, it follows a higher-energy equilibrium path, which results in a higher peak moment.

This difference in behavior is not surprising, as thin shell structures exhibit multiple energetically-similar equilibrium paths [43], and the choice between different paths is very sensitive to small geometric imperfections in the structure.

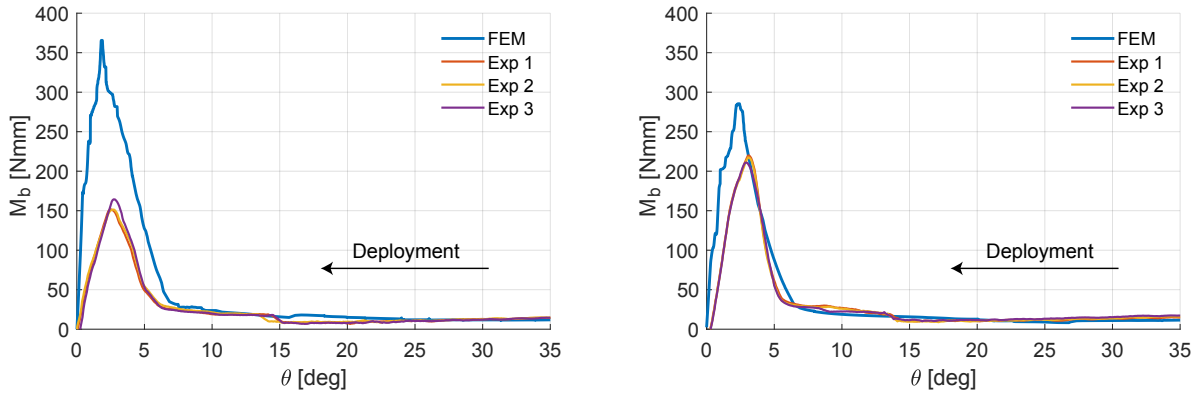

(a) Strip 1, without membrane

(b) Strip 2, with membrane

Fig. 16 Comparison between simulations and experiments for quasi-static deployment.

Therefore, since no imperfections were introduced in the simulation, the model follows the most symmetric equilibrium solution, which is not necessarily the lowest energy path. For the same reason, in the simulation the localized folds on the two longerons disappear at the same time, but in the experiment this only happens for the strip with the membrane. This explains why the error is smaller in this case. This result suggests that the coupling between the longerons introduced by the membrane makes the structure less sensitive to imperfections, leading to a more deterministic and predictable behavior.

Although the numerical model of the moment-rotation relation for the strip is not in good agreement with the measured response for small rotations, No correction of the peak moments was introduced in the deployment simulations presented in this paper, as the steady-state moment for fold angles larger than 7° is predicted with an error smaller than 10% RMS error it captures with sufficient accuracy the steady-state moment. It is this value of the moment that drives most of the unfolding of the strip. Specifically, the fold angle becomes smaller than 7° in the final 5% of the deployment time. A correction of the peak moment could be introduced to better model the latching of the elastic folds.

B. Comparison of Deployment Results

The results of the deployment simulations for the two strips have been compared to the experimental results in Sec. IV. The plots in Figs. 17-18 present the evolution of the fold angle, whose values were obtained from the experiments as explained in Sect. IV. To obtain the fold angles from the finite element simulations, the coordinates of the nodes along the inner edge of the longeron webs were extracted at each increment of the solution. Then, the algorithm described in Sect. IV was used to compute the distribution of longitudinal curvature, identify the location of the elastic folds, calculate the local orientation along the longerons, and define the fold angle as the median of such orientation in the region between the folds and the ends of the longerons. The height of the center of the strip as a function of time was also obtained. Green and blue lines correspond to the experimental data for the two longerons; red lines represent

simulations. Different runs of the same experiment are indicated by solid, dashed and dotted lines.

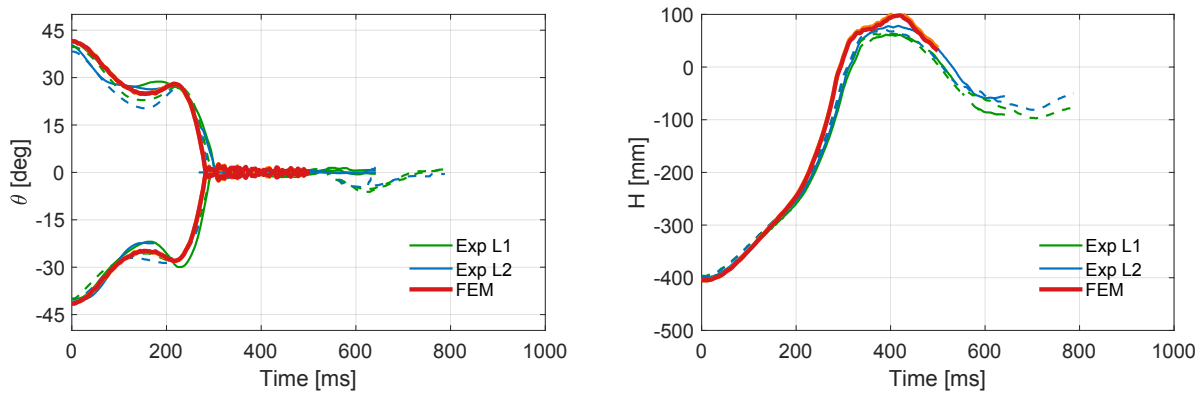

(a) Fold angles

(b) Center height

Fig. 17 Comparison between experiments in vacuum and simulations for strip without membrane.

Figure 17 shows the results for the strip without membrane. The simulation closely matches the experiments. The fold angles decrease symmetrically for both longerons, and hence only one longeron has been plotted. The amplitude and period of the oscillation of the fold angle are well captured by the simulation, and the deployment time is 4% slower than the mean deployment time from the experiments. When the fold angles become zero for the first time, latching of the longerons occurs and the strip starts vibrating. Figure 17(b) shows the evolution of the height of the center of the strip. The simulation and the experiments start from the same height (400 mm below the position of the pulleys), and closely match for the initial 250 ms of deployment, with a 8.5 mm RMS error. After this time, the simulation becomes faster than the experiment, crossing the equilibrium position ($z = 0$) 15 ms before and reaching a 30 mm higher peak height.

Figures 18(a) and 18(b) show the results for the strip with membrane, deploying in vacuum. Again, there is good agreement between simulation and experiments, with the predicted fold angle being within the envelope of experimentally measured angles, and the predicted deployment time being less than 5% slower than the mean experimental value. Regarding the height of the center of the strip, the simulation starts from the same value as the experiment, but becomes slightly slower after 150 ms, maintaining a 30 mm constant offset after this point. However, at the end of deployment, it reaches the same maximum height at approximately the same time.

Figures 18(c) and 18(d) present the results for the strip with membrane deploying in air. The simulation correctly captures the amplitude and period of the oscillation in the fold angle, as well as the deployment time. Because of the symmetry assumption in the finite element model, the two folds on each longeron disappear at the same time, whereas in the experiments there is an average delay of 50 ms, possibly due to geometric imperfections and/or initial pre-stress in the Kapton membrane. A very good agreement is also found in the evolution of the height of the center of the strip, Fig. 18(d), throughout the entire deployment.

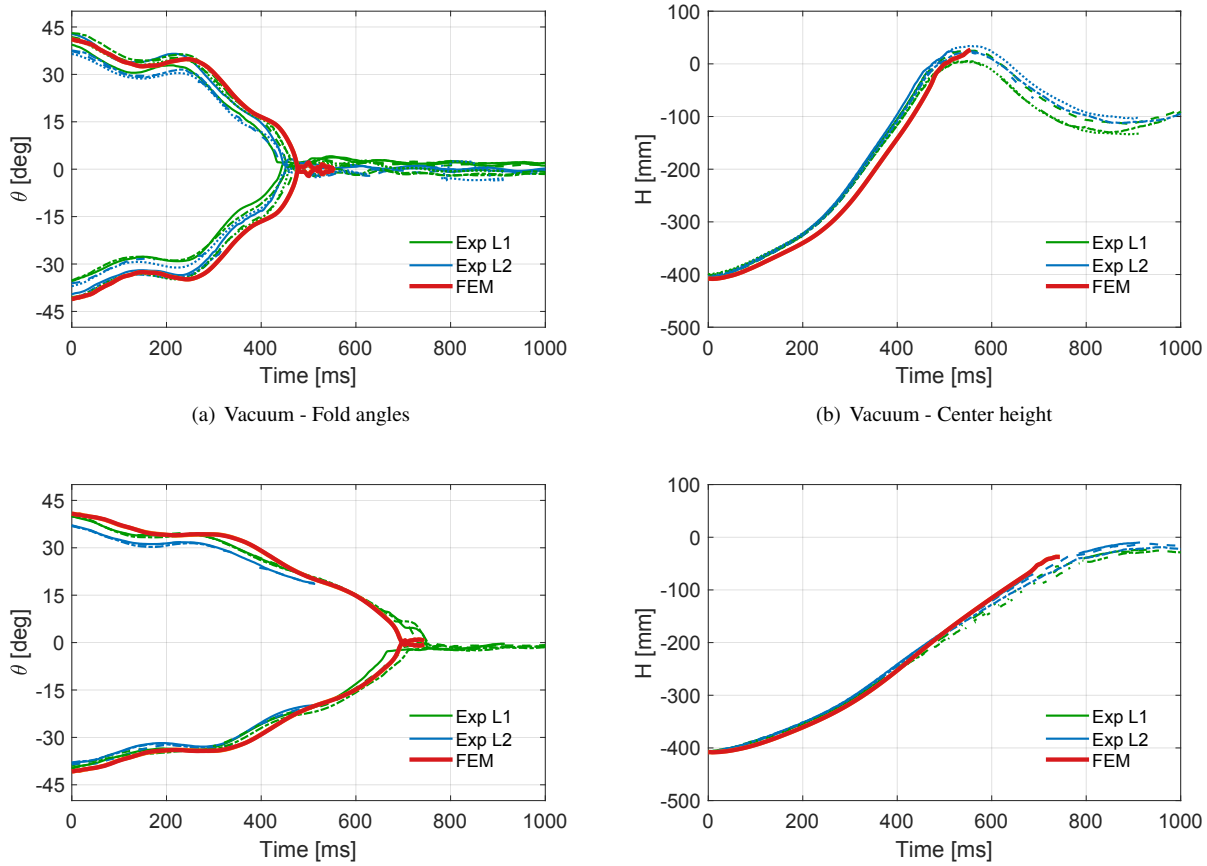

(a) Vacuum - Fold angles

(b) Vacuum - Center height

(c) Air - Fold angles

(d) Air - Center height

Fig. 18 Comparison between experiments and simulations for strip with membrane.

VII. Discussion and Conclusion

This paper has presented a study of the dynamic deployment of rectangular space frames composed of interconnected, ultralight thin-shell longerons. The structures were initially folded by forming two elastic folds, and were then deployed by releasing the stored elastic energy. An experimental setup was designed to symmetrically fold 1.125 m long prototypes, which were supported by a cord suspension system and deployed against gravity with the assistance of two edge masses. DIC was used to measure the deformation of the structure during deployment and an algorithm, robust against noisy and incomplete point clouds, was developed to track the location and angle of the elastic folds. The algorithm, implemented in MATLAB, can be adapted to different shell geometries and to point clouds obtained from different measurement techniques, and is available to the interested reader at the following link `https://github.com/apedivel/thin_shell_localized_folds.git`.

Deployment experiments have shown that a symmetrically folded structure remains essentially symmetric during the deployment process. For the particular experiments presented in the paper, the elastic folds did not move along the longerons, behaving as non-linear elastic hinges. In experiments with different initial locations for the elastic folds (very

close to the center or to the ends of the strips), not presented in this paper but available in [10], the folds did move, although they were often constrained by the battens to remain within one bay of the structure.

The effect of air on the deployment dynamics has been experimentally characterized for the first time. It has been shown that the interaction with air significantly slows down the deployment of the strip supporting a thin membrane. However, this effect becomes negligible in the absence of the membrane.

The finite-element simulation of packaging and deployment has been validated first for the case of a quasi-static deployment, where it was able to correctly predict the steady-state moment of the strip prototypes, but overpredicted the peak moments at the end of deployment, due to the sensitivity of the longerons to local variations of the flange radius and angle. The effects of such imperfections have been studied elsewhere [43]. The dynamic deployment simulations have correctly captured the folded configuration, and accurately predicted the evolution of the fold angles during deployment, with less than 5 % error on the deployment time. Simple models to estimate the added mass of air from the geometry of the structure, as well as air drag have been proposed. Simulations based on these models closely match the deployment behavior observed in the experiments.

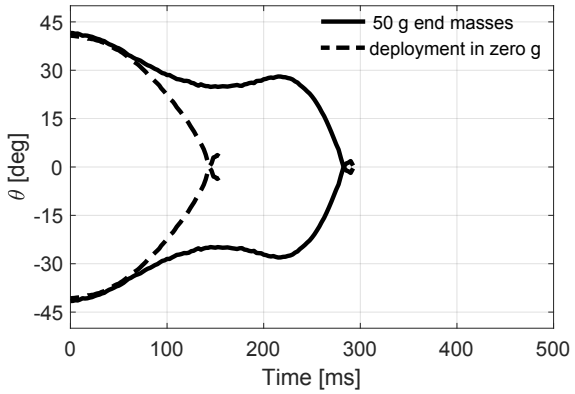

Fig. 19 Effect of gravity on strip deployment.

The presented simulation method can be used to predict the effects of different loads and boundary conditions on the deployment of thin shell structures. Figure 19, obtained from simulations, compares the evolution of the elastic folds $\theta(s)$ in a strip without membrane that deploys under gravity with a suspension system including 50 g end masses to the same strip, but without the gravity compensation system, deploying in zero-g. This plot shows that the deployment in zero-g would be almost twice as fast as deployment under gravity. Also, in zero-g the angles of the folds decrease monotonically, whereas for the gravity deployment case they oscillate in the final part of deployment. These differences are mainly due to the inertia of the end masses, which slow down the deployment of the strip and cause the oscillation of the elastic folds. It would be possible to build on these results and design suspension systems that highlight different features of the deployment process.

In conclusion, it has been shown that the packaging and deployment of space frames consisting of thin-shell

longerons can be reliably tested in the lab and can also be simulated accurately. This result opens a promising path forward for the application of thin shell technologies to novel deployable structures. An application of the modeling techniques presented in this paper to novel SSPP structures consisting of multiple strips that dynamically self-deploy and latch will be presented in a follow-on publication.

Acknowledgements

The authors thank Professor Xiaowei Deng (University of Hong Kong) for providing the Abaqus/Explicit implementation of the IMP membrane formulation, Alan Truong (Caltech) for building the strip prototypes and Fabien Royer (Caltech) for help with the bending tests. Financial support from the Space Solar Power Project at Caltech is gratefully acknowledged.

References

[1] Wu, S.C., and Ghofranian, S., "Anomaly simulation and resolution of International Space Station solar array deployment," Modeling, Simulation, and Verification of Space-based Systems II, Vol. 5799, 2005, pp. 38–48.

[2] Klesh, A., and Krajewski, J., "MarCO: CubeSats to Mars in 2016," Proceedings of the 29th Annual AIAA/USU Conference on Small Satellites, 2015.

[3] Sauder, J. F., Arya, M., Chahat, N., Shi, M., Agnes, G., and Cwik, T.,"Deployment mechanisms for high packing efficiency one-meter reflectarray antenna (OMERA),"AIAA Scitech 2019 Forum, 2019.

[4] Hausgen, P. E., Carpenter, B., Gupta, N., and Turse, D., "TacSat 2 experimental solar array on-orbit data and analysis", 2016 IEEE 43rd Photovoltaic Specialists Conference (PVSC), 2016, pp. 2565–2570. DOI: 10.1109/PVSC.2016.7750111 .

[5] Spence, B. R., White, S., LaPointe, M., Kiefer, S., LaCorte, P., Banik, J., Chapman, D., and Merrill, J., "International space station (ISS) roll-out solar array (ROSA) spaceflight experiment mission and results," 2018 IEEE 7th World Conference on Photovoltaic Energy Conversion (WCPEC), IEEE, 2018, pp. 3522–3529. 10.1109/PVSC.2018.8548030 .

[6] Ikeya, K. et al., "Significance of 3U CubeSat OrigamiSat-1 for space demonstration of multifunctional deployable membrane," Acta Astronautica, 2020, 173, 363-377. https://doi.org/10.1016/j.actaastro.2020.04.016 .

[7] Yang, D., Yang, R., Priya, S., and Liu, S., "Recent advances in flexible perovskite solar cells: fabrication and applications," Angewandte Chemie International Edition, Vol. 58, No. 14, 2019, pp. 4466–4483. https://doi.org/10.1002/anie.201809781 .

[8] Hashemi, M. R. M., Fikes, A. C., Gal-Katziri, M., Abiri, B., Bohn, F., Safaripour, A., Kelzenberg, M. D., Warmann, E. L., Espinet, P., Vaidya, N., Gdoutos, E. E., Leclerc, C., Royer, F., Pellegrino, S., Atwater, H. A., and Hajimiri, A., "A flexible phased array system with low areal mass density," Nature Electronics, Vol. 2, No. 5, 2019, pp. 195–205. https://doi.org/10.1038/s41928-019-0247-9 .

[9] Arya, M., Lee, N. and Pellegrino, S. "Ultralight Structures for Space Solar Power Satellites," SciTech 2016, 2016 San Diego, AIAA-2016-1950.

[10] Pedivellano, A., "Deployment Dynamics of Thin-Shell Space Structures", Ph.D. Thesis, California Institute of Technology, 2021.

[11] Seffen, K., and Pellegrino, S., "Deployment dynamics of tape springs," Proceedings of the Royal Society of London. Series A: Mathematical, Physical and Engineering Sciences, Vol. 455, No. 1983, 1999, pp. 1003–1048. https://doi.org/10.1098/rspa.1999.0347 .

[12] Mallikarachchi, H., and Pellegrino, S., "Deployment dynamics of ultrathin composite booms with tape-spring hinges," Journal of Spacecraft and Rockets, Vol. 51, No. 2, 2014, pp. 604–613. https://doi.org/10.2514/1.A32401 .

[13] Royer, F., and Pellegrino, S., "Ultralight ladder-type coilable space structures," 2018 AIAA Spacecraft Structures Conference, 2018-1200.

[14] Roybal, F., Banik, J., and Murphey, T., "Development of an elastically deployable boom for tensioned planar structures," 48th AIAA/ASME/ASCE/AHS/ASC Structures, Structural Dynamics, and Materials Conference, 2007-1838.

[15] Lekan, J., "Microgravity research in NASA ground-based facilities," 27th Aerospace Sciences Meeting, 1989-236.

[16] Steinberg, T., "Reduced gravity testing and research capabilities at Queensland University of Technology's New 2.0 Second Drop Tower," Advanced Materials Research, Vol. 32, Trans Tech Publ, 2008, pp. 21–24.

[17] Block, J., Bäger, A., Behrens, J., Delovski, T., Hauer, L.-C., Schütze, M., Schütze, R., and Spröwitz, T., "A self-deploying and self-stabilizing helical antenna for small satellites," Acta Astronautica, Vol. 86, 2013, pp. 88–94. https://doi.org/10.1016/j.actaastro.2011.10.012 .

[18] Firth, J., Adamcik, B., Hannah, E., Firth, D., and Pankow, M., "Minimal Unpowered Strain-Energy Deployment Mechanism for Rollable Spacecraft Booms," AIAA Scitech 2019 Forum, 2019-1258.

[19] Mao, H., Ganga, P. L., Ghiozzi, M., Ivchenko, N., and Tibert, G., "Deployment of bistable self-deployable tape spring booms using a gravity offloading system," Journal of Aerospace Engineering, Vol. 30, No. 4, 2017-04017007, https://doi.org/10.1061/(ASCE)AS.1943-5525.0000709 .

[20] Fischer, A., and Pellegrino, S., "Interaction between gravity compensation suspension system and deployable structure," Journal of Spacecraft and Rockets, Vol. 37, No. 1, 2000, pp. 93–99.

[21] Greschik, G., and Belvin, W. K., "High-fidelity gravity offloading system for free-free vibration testing," Journal of Spacecraft and Rockets, Vol. 44, No. 1, 2007, pp. 132–142. DOI: 10.2514/1.21454 .

[22] Leclerc, C., Pedivellano, A., and Pellegrino, S., "Stress concentration and material failure during coiling of ultra-thin TRAC booms," 2018 AIAA Spacecraft Structures Conference, 2018-0690.

[23] Leclerc, C., and Pellegrino, S., "Nonlinear elastic buckling of ultra-thin coilable booms," International Journal of Solids and Structures, Vol. 203, 2020, pp. 46–56. https://doi.org/10.1016/j.ijsolstr.2020.06.042 .

[24] Royer, F., Li, Y., Truong, A., Sommer, C., and Pellegrino, S., "Pure Bending Machine for Testing Non-Linear Structures," In preparation.

[25] Houpert, L., "Ball bearing and tapered roller bearing torque: analytical, numerical and experimental results," Tribology Transactions, Vol. 45, No. 3, 2002, pp. 345–353. https://doi.org/10.1080/10402000208982559 .

[26] Maronna, R. A., Martin, R. D., Yohai, V. J., et al., Robust statistics: theory and methods (with R), John Wiley & Sons, 2019.

[27] Jolliffe, I.T., 2003. Principal component analysis. Technometrics, 45(3), p. 276. https://doi.org/10.1002/0470013192.bsa501 .

[28] Helfrick, M.N., Niezrecki, C., Avitabile, P., and Schmidt, T., "3D digital image correlation methods for full-field vibration measurement", Mechanical Systems and Signal Processing, Vol. 25, 2011, pp. 917–927. https://doi.org/10.1016/j.ymssp.2010.08.013 .

[29] Miller, R. K., and Hedgepeth, J. M., "An algorithm for finite element analysis of partly wrinkled membranes," AIAA Journal, Vol. 20, No. 12, 1982, pp. 1761–1763. https://doi.org/10.2514/3.8018 .

[30] Miller, R. K., Hedgepeth, J. M., Weingarten, V. I., Das, P., and Kahyai, S., "Finite element analysis of partly wrinkled membranes," Advances and Trends in Structures and Dynamics, Elsevier, 1985, pp. 631–639.

[31] Adler, A., and Mikulas, M., "Application of a wrinkled membrane finite element approach to advanced membrane structures," AIAA Space 2001 Conference and Exposition, 2001-4646.

[32] Deng, X., and Pellegrino, S., "Wrinkling of orthotropic viscoelastic membranes," AIAA Journal, Vol. 50, No. 3, 2012, pp. 668–681. DOI: 10.2514/1.J051255 .

[33] Aufaure, M., "A finite element of cable passing through a pulley," Computers & Structures, Vol. 46, No. 5, 1993, pp. 807–812. https://doi.org/10.1016/0045-7949(93)90143-2 .

[34] Ju, F., and Choo, Y. S., "Dynamic analysis of tower cranes," Journal of Engineering Mechanics, Vol. 131, No. 1, 2005, pp. 88–96. https://doi.org/10.1061/(ASCE)0733-9399(2005)131:1(88) .

[35] Fraterman, E., and Lupker, H., "Evaluation of belt modelling techniques," Tech. rep., SAE Technical Paper, 1993.

[36] Hughes, K., Gulavani, O., Vuyst, T. D., and Vignjevic, R., "Explicit dynamic formulation to demonstrate compliance against quasi-static aircraft seat certification loads (CS25. 561)–Part II: Influence of body blocks," Proceedings of the Institution of Mechanical Engineers, Part G: Journal of Aerospace Engineering, Vol. 228, No. 10, 2014, pp. 1890–1903. https://doi.org/10.1177/0954410013506415 .

[37] Yasaka, T., and Oda, S., "Air effects on the structure vibration and the considerations to large spacecraft ground testing," 39th Congress of the International Astronautical Federation, 1988.

[38] Kukathasan, S., and Pellegrino, S., "Vibration of prestressed membrane structures in air," 43rd AIAA/ASME/ASCE/AHS/ASC Structures, Structural Dynamics, and Materials Conference, AIAA 2002-1368.

[39] Sewell, J., Miserentino, R., and Pappa, R. S., "Vibration studies of a lightweight three-sided membrane suitable for space application," NASA Technical Paper 2095, 1983.

[40] Sygulski, R., "Dynamic analysis of open membrane structures interacting with air," International Journal for Numerical Methods in Engineering, Vol. 37, No. 11, 1994, pp. 1807–1823. https://doi.org/10.1002/nme.1620371103 .

[41] Lindsey, W., "Drag of cylinders of simple shapes," NACA Technical Report, Vol. 619, 1938, pp. 169–176.

[42] Sakovsky, M., and Pellegrino, S., "Closed cross-section dual-matrix composite hinge for deployable structures," Composite Structures, Vol. 208, 2019, pp. 784–795. https://doi.org/10.1016/j.compstruct.2018.10.040 .

[43] Royer, F., and Pellegrino, S., "Buckling of ultralight ladder-type coilable space structures", SciTech 2020, AIAA-2020-1437.